Electronic Supplementary Material (ESI) for Nanoscale.

Galenic Lab-on-a-Chip concept for lipid nanocapsules production

Nicolas ROLLEY[a], Marie BONNIN[a], Guillaume LEFEBVRE[a], Sylvain VERRON[b], Sylwester BARGIEL[c], Laurent ROBERT[c], Jérémie RIOU[a], Carl SIMONSSON[a], Thomas BIZIEN[d], Jean-Christophe GIMEL[a], Jean-Pierre BENOIT[a], Guillaume BROTONS[e], Brice CALVIGNAC[a]

Supporting Information

S1 Galechip pilot ***.....2***

S2 Chips design ***.....3***

S3 Chip Plugging and heating devices manufactured by 3D printing ***.....4***

S4 Digital microscopy on the different chips for channel characteristic measurements ***.....6***

S5 Confocal laser scanning microscope on PEEK chip for channel characteristic measurements ***.....11***

S6 Statistical analysis ***.....12***

- **PEEK vs Si/Glass** **.....12**
- **Low vs High flow rate** **.....13**

S7 Small Angle X-ray Scattering (SAXS) data treatment and comparison ***.....16***

S1 Galechip pilot

Figure S1-1 and Figure S1-2 present the main elements of the home-made Galechip pilot.

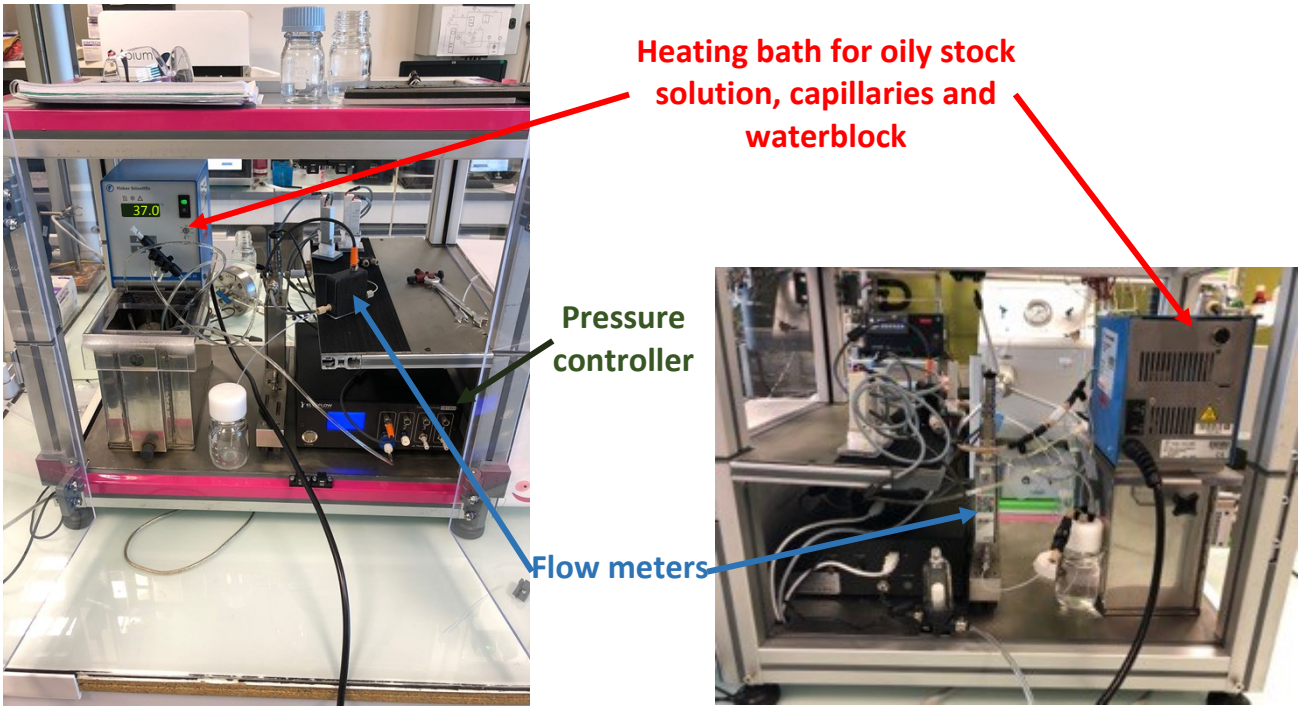

Figure S1-1: Global overview of the Galechip Pilot

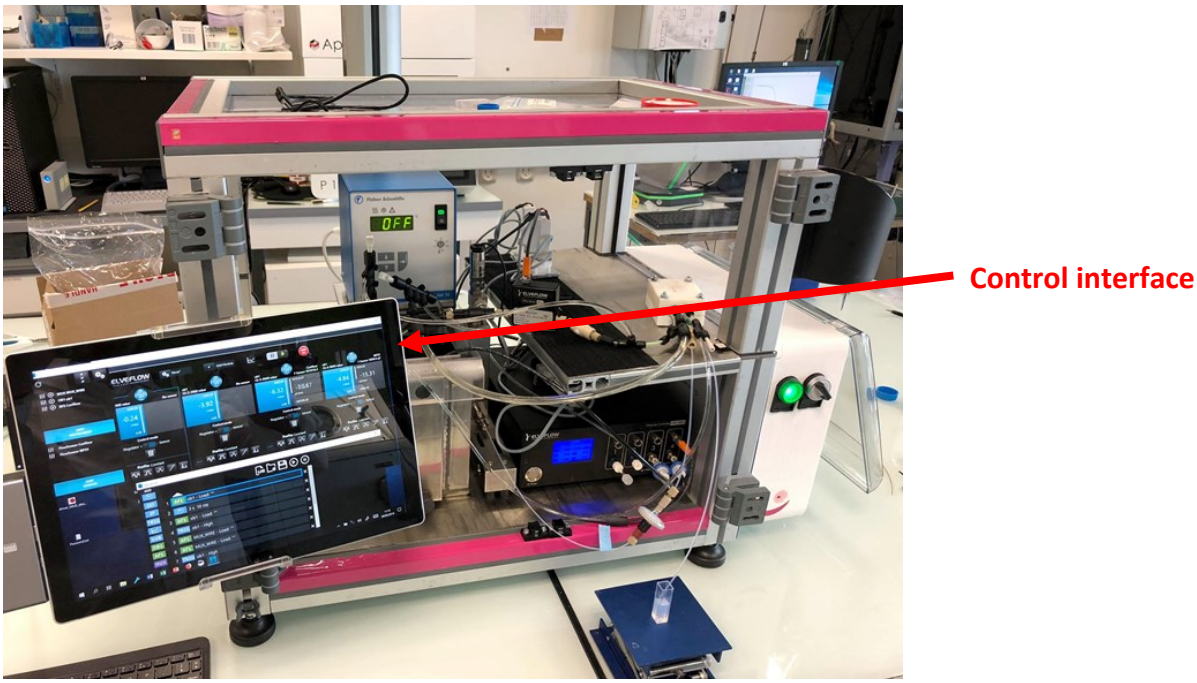

Figure S1-2: Galechip pilot for Lipid Nanocapsule production

S2 Chips design

The additive manufacturing of ABS (Verbatim Gmbh, Eschborn, Germany) and PEEK (Apium Additive Technologies Gmbh, Karlsruhe, Germany) chips require four steps (Figure S2-1):

(A) The 3D chip design was modelled with a CAD software at the same dimensions as the Si/Glass chip, except for the channel section because of the limited resolution of the 3D printer. This led to a shorter channel length and less elbows. However, the fluid volume of the 3D printed chip was similar. All specifications of 3D printed chips are summarized in Table S2-1 in parallel with those of the Si/Glass chips.

(B) A slicing step, carried out with Simplify3D v4.1.1 (Cincinnati, USA), turns the 3D model into 2D slices to be processed by the printer. To avoid the warping phenomena during the printing (a classical 3D printing issue caused by the shrinkage of corners that leave the build plate during the printing, deforming the all printed object), twelve retaining support ribs were added around the chip (three on each side of the chip, located on critical locations, see Fig. 2B).

(C) The 3D printing of polymer microfluidic chips was carried out with the FDM technology using a P220 3D printer (Apium Additive Technologies Gmbh, Karlsruhe, Germany) for PEEK and a U20 3D Printer (Alfawise, Shenzhen, China) for ABS. The P220 3D printer was used with a 0.4 mm diameter nozzle at 480°C to extrude a 1.75 mm diameter PEEK filament. The fused filament was deposited on a 205 × 155 mm thermalized bed kept at 130°C. The U20 3D printer was used with a 0.4 mm diameter nozzle at 245°C to extrude a 1.75 mm diameter ABS filament. The fused filament was deposited on a 300 x 300 mm thermalized bed kept at 93°C.

(D) To obtain a functional chip, a machining step was needed. Retaining ribs were removed, and the chip surface was sanded. A FF230 milling machine (Proxxon SA, Wecker, Luxembourg) was used to drill 300 µm holes. The last step consisted in smoothing horizontal surfaces to eliminate potential leaks once the chip is integrated in the plugging device due to a surface rugosity.

Table S2-1 presents the targeted geometrical characteristics of the three used chips. The chip external sizes are similar so that they can be used with the same connectors and waterblock, but channel widths are different due to the limited resolution of 3D printers, resulting in a shorter total length but similar filling volume.

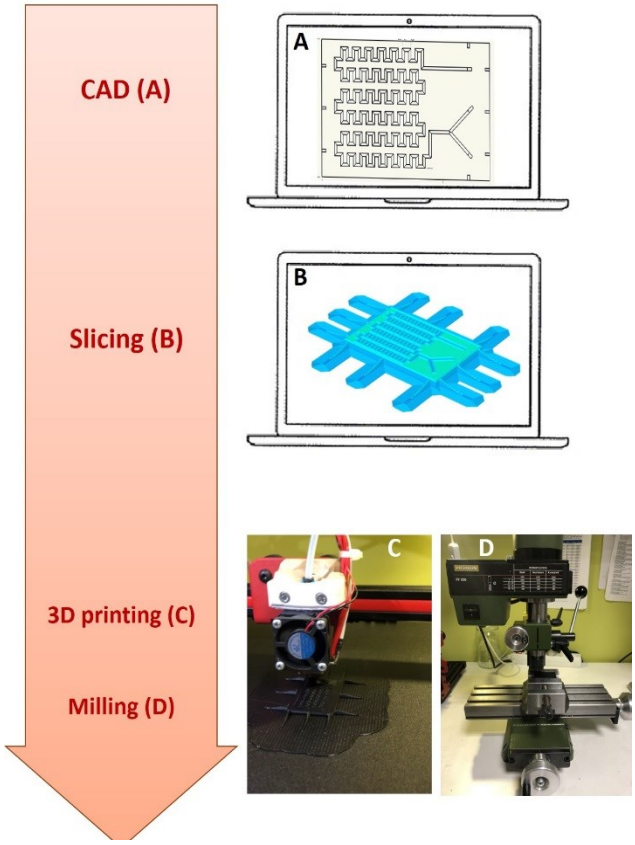

Fig S2-1: Flowchart for the chips manufacturing process. (A) CAD drawing. (B) Slicing of the CAD Drawing. (C) Printing of the chip (The Alfawise® 3D Printer used for the ABS printing is depicted on the picture). (D) Milling of the chip. (See section S2 for details)

Table S2-1: Geometrical characteristics of Si/Glass chip and 3D printed chips (ABS and PEEK)

	Si/Glass Chip	**ABS and PEEK 3D printed Chips**
Shape	Rectangle	Rectangle
Length	40 mm	40 mm
Width	26 mm	26 mm
Thickness	2.3 mm	2.6 mm
Channel design	"Y" junction (2 inlets and 1 outlet) with a 90° angle	"Y" junction (2 inlets and 1 outlet) with a 90° angle
Channel section	Rectangular: 300 x 1,500 µm	Rectangular: 600 x 1,500 µm
Mixing section	607 elbows with 90° angles	172 elbows with 90° angles
Channels total length	500 mm (including 453.46 mm from mixing point)	334.04 mm (including 318.65 mm from mixing point)

S3 Chip Plugging and heating devices manufactured by 3D printing

The water circulation chamber was covered with an aluminum heat-conducting plate to optimize heat transfers between the circulating water and the chip (Fig. 3B in the article). The fluidic connectors (part (2) in Fig. 3A and 3B in the article) were composed of two inlets and one outlet which were tapped in 10/32 to connect capillaries and

sealed with o-rings (Fig. S3-1). Each channel was drilled with a Ø 400 µm hole. An L-shaped window was designed on the waterblock and the connector part to enable the X-Ray beam path (part (3) on Fig. 3C in the article). This L-shaped window coincided with the Y injection and many elbows of the integrated chip (zoom on Fig. 3C – more information on the SAXS implementation in section 2.5.2 SAXS analysis in the article). The waterblock and the connector part were designed using a CAD drawer and prototyped with the OBJET30 3D inkjet printer (Stratasys, Eden Prairie, USA). The 3D printing material used for both parts was the VeroWhitePlus RGD835 (Stratasys, Eden Prairie, USA) which was processed at a temperature below 48°C. Plugging and heating devices have been printed with 3D inkjet printing technology to ensure a good printing resolution of the seal groove, and of fluidic channels between plugs and chip.
Figure S3-1 shows the different parts of the waterblock device presented in section 2.3 in the article.

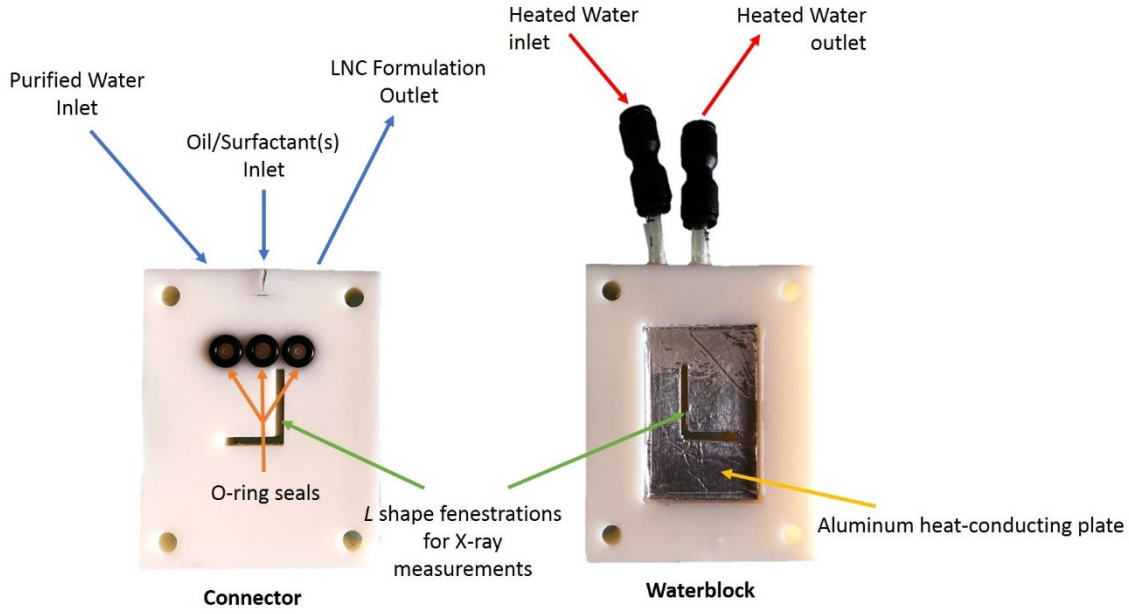

Figure S3-1: Details of the "all-in-one" plugging and heating device parts

S4 Digital microscopy on the different chips for channel characteristic measurements

Digital microscopy has been performed on the Si/Glass, ABS and PEEK chips. The results are presented in the main text (section 3.1.2 and Fig. 6). The following figures complete these results, presenting the measurement performed in each of the five regions of interest (ROI) for four different chips:

- A Si/Glass chip with its glass cover (Figure S4-1)
- A Si/Glass chip without glass cover (to confirm that the glass cover does not impact measurements): only one point is shown here and the chip design is different but repeatability of the DRIE process has been controlled on different design – data not shown) (Figure S4-2)
- An ABS chip (Figure S4-3)
- A PEEK chip (Figure S4-4)

Reproducibility of the fabrication processes (DRIE and 3D printing) have been controlled by doing the same measurements on different chips (data not shown).

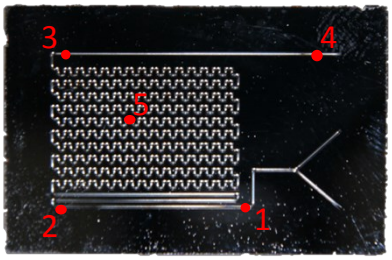

ROI 5	Channel 1	Channel 2	Channel 3	Channel 4	Channel 5
Length (µm)	1,421.89	1,434.11	1,436.99	1,439.65	1,438.89
Width (µm)	280.14	269.85	270.12	271.65	265.10
Angle (Deg) (L / R)	92.63 / 88.21	89.25 / 91.09	93.62 / 86.90	92.08 / 88.26	89.99 / 90.77

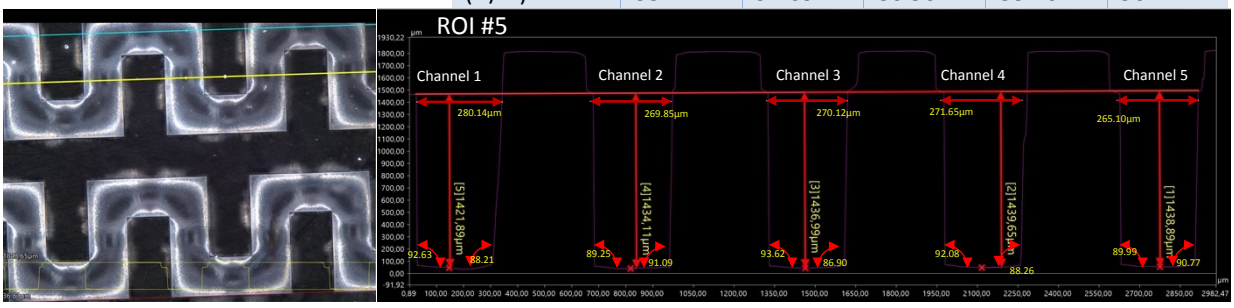

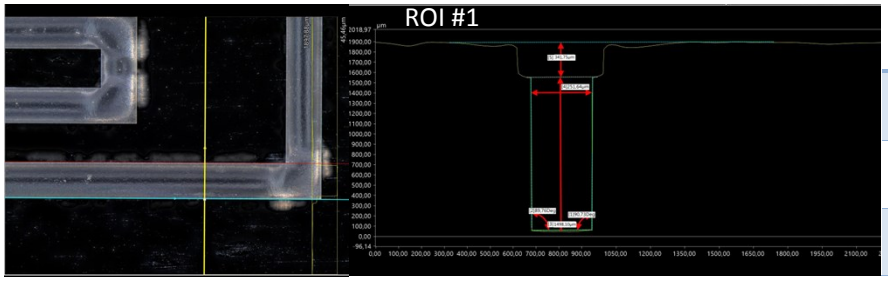

ROI 1	Channel 1
Length (µm)	1,498.10
Width (µm)	251.64
Angle (Deg) (L / R)	89.70 / 90.73

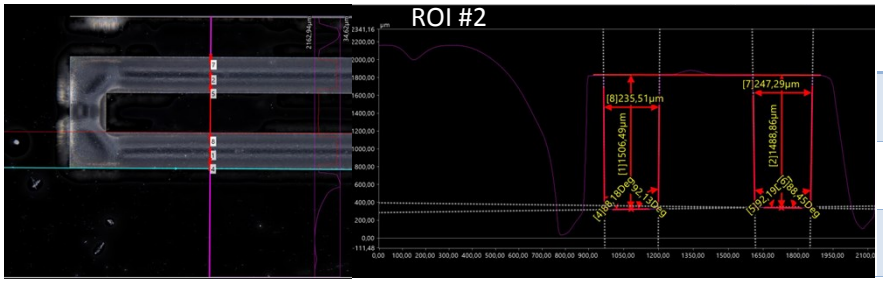

ROI 2	Channel 1	Channel 2
Length (µm)	1,506.49	1,488.86
Width (µm)	235.51	247.29
Angle (Deg) (L / R)	88.18 / 92.13	92.19 / 88.45

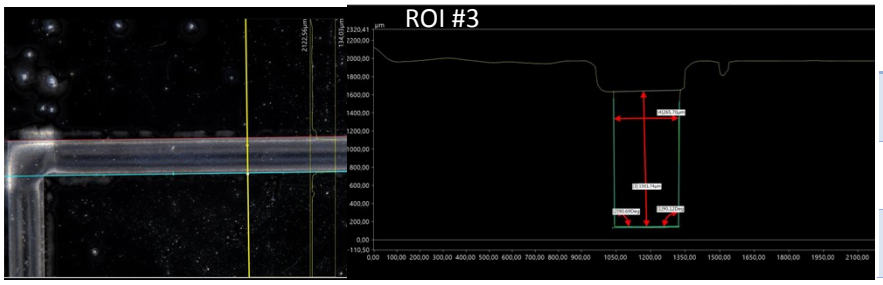

ROI 3	Channel 1
Length (µm)	1,501.74
Width (µm)	265.70
Angle (Deg) (L / R)	90.69 / 90.12

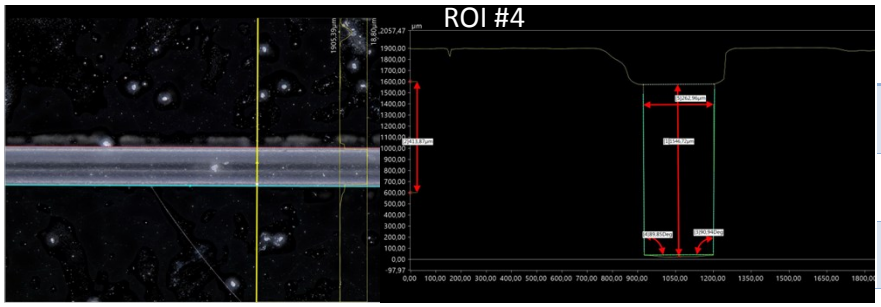

ROI 4	Channel 1
Length (µm)	1,546.72
Width (µm)	262.96
Angle (Deg) (L / R)	89.85 / 90.94

Figure S4-1: Digital microscopy observations of the Si/Glass chip with its glass cover: whole chip (including the localization of the 5 ROI) and zoom on each of the ROI, completed with the software measurement windows and tables with the obtained values.

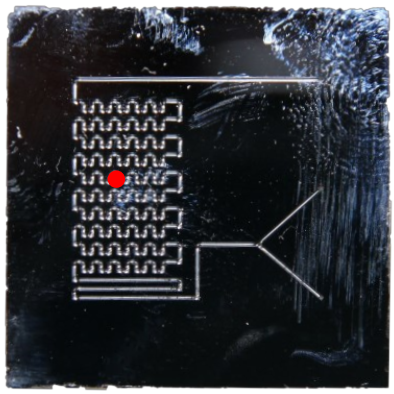

ROI 5	Channel 1	Channel 2	Channel 3	Channel 4
Length (µm)	1,477.68	1,481.71	1,479.30	1,470.59
Width (µm)	284.52	275.18	277.40	276.75
Angle (Deg) (L / R)	90.45 / 90.01	90.45 / 90.03	90.45 / 89.87	90.45 / 89.95

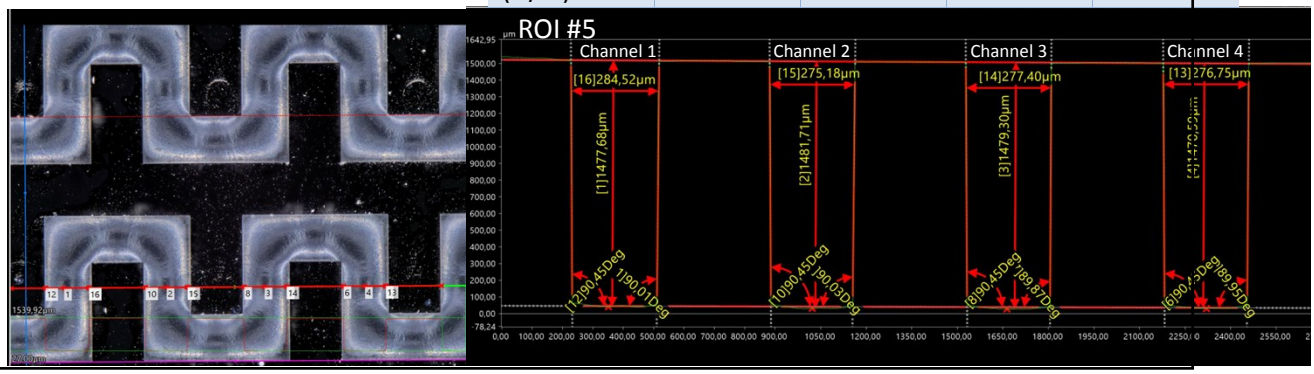

Figure S4-2: Digital microscopy observations of the Si/Glass chip without its glass cover: whole chip (including the localization of the ROI 5) and zoom on this ROI, completed with the software measurement windows and table with the obtained values.

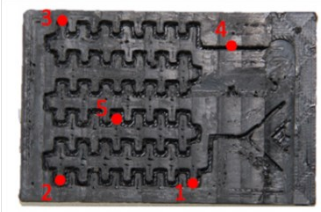

ROI 1		Channel 1	Channel 2
Length (µm)		1,623.62	1,611.89
Width (µm)	Top	430.78	482.78
	Down	218.88	390.62
Angle (Deg) (L / R)		N/A	N/A

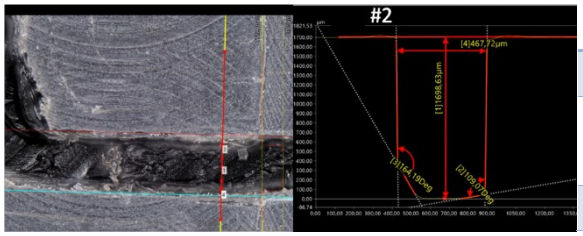

ROI 2		Channel 1
Length (µm)		1,6298.63
Width (µm)	Top	467.72
	Down	-
Angle (Deg) (L / R)		N/A

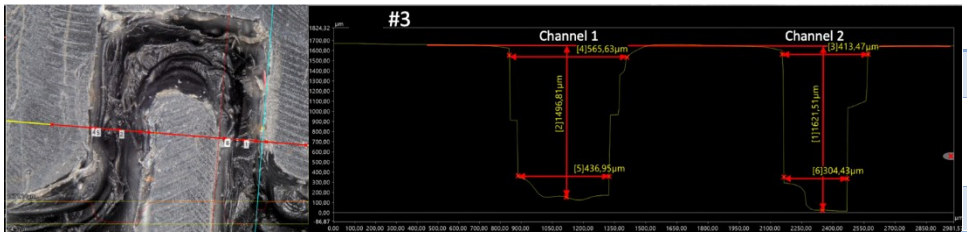

ROI 3		Channel 1	Channel 2
Length (µm)		1,496.81	1,621.51
Width (µm)	Top	565.63	413.47
	Down	436.95	304.43
Angle (Deg) (L / R)		N/A	N/A

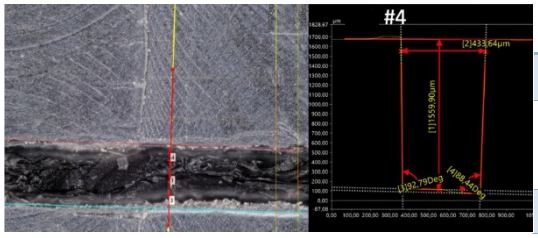

ROI 4		Channel 1
Length (µm)		1,559.90
Width (µm)	Top	433.64
	Down	-
Angle (Deg) (L / R)		92.79 / 88.44

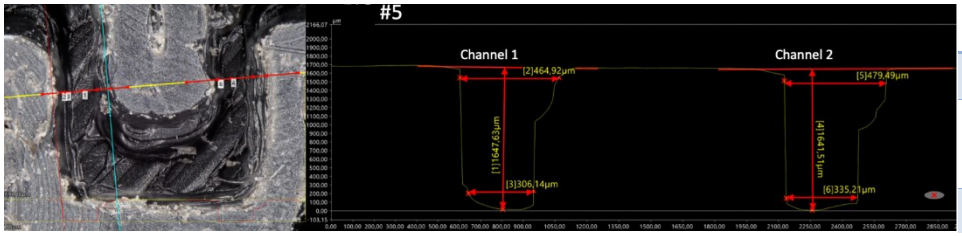

ROI 5		Channel 1	Channel 2
Length (µm)		1,647.63	1,641.51
Width (µm)	Top	464.92	479.49
	Down	306.14	335.21
Angle (Deg) (L / R)		N/A	N/A

Figure S4-3: Digital microscopy observations of the ABS chip: whole chip (including the localization of the 5 ROI) and zoom on each of the ROI, completed with the software measurement windows and tables with the obtained values.

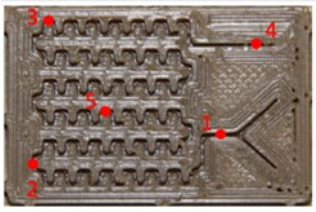

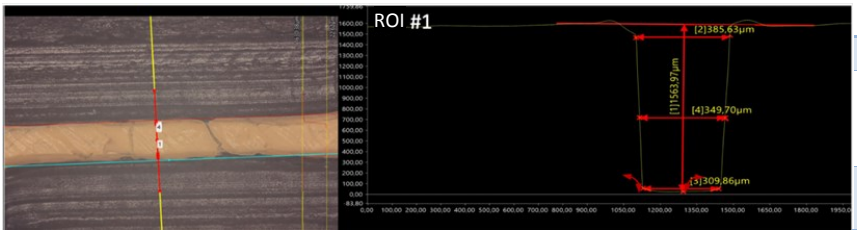

ROI 1		Channel 1
Length (µm)		1,563.97
Width (µm)	Top	385.63
	Middle	349.70
	Down	309.86
Angle (Deg) (L / R)		90.77 / 94.12

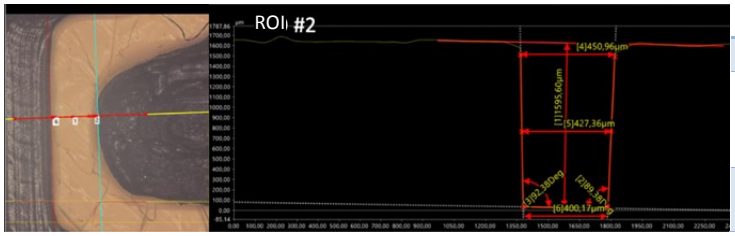

ROI 2		Channel 1
Length (µm)		1,595.60
Width (µm)	Top	450.96
	Middle	427.36
	Down	400.17
Angle (Deg) (L / R)		93.38 / 89.38

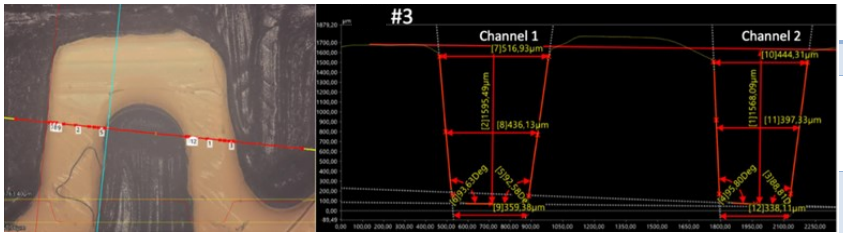

ROI 3		Channel 1	Channel 2
Length (µm)		1,594.49	1,568.09
Width (µm)	Top	516.93	444.31
	Middle	436.13	397.33
	Down	359.38	338.11
Angle (Deg) (L / R)		93.63 / 92.58	95.80 / 88.81

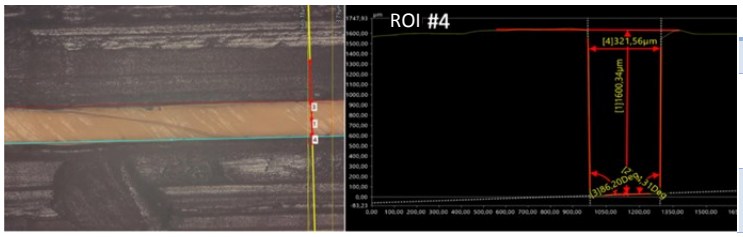

ROI 4		Channel 1
Length (µm)		1,600.34
Width (µm)	Top	321.56
	Middle	
	Down	
Angle (Deg) (L / R)		86.20 / 94.34

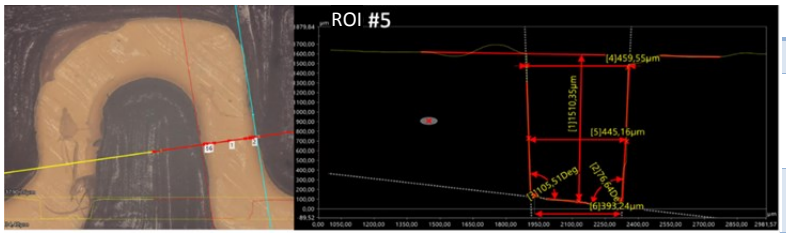

ROI 5		Channel 1
Length (µm)		1,510.34
Width (µm)	Top	449.55
	Middle	445.17
	Down	393.24
Angle (Deg) (L / R)		105.51 / 76.64

Figure S4-4: Digital microscopy observations of the PEEK chip: whole chip (including the localization of the 5 ROI) and zoom on each of the ROI, completed with the software measurement windows and tables with the obtained values.

S5 Confocal laser scanning microscope on PEEK chip for channel characteristic measurements

Thanks to PEEK autofluorescence, PEEK chip has also been characterized by confocal laser scanning microscope on two ROI (Figure S5-1, Figure S5-2, Figure S5-3)

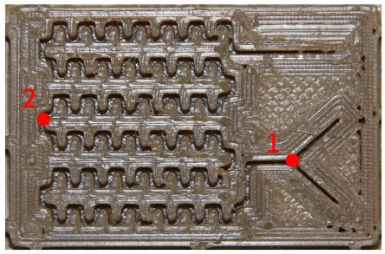

Figure S5-1: PEEK chip overall view with the two ROI observed by confocal laser scanning microscope

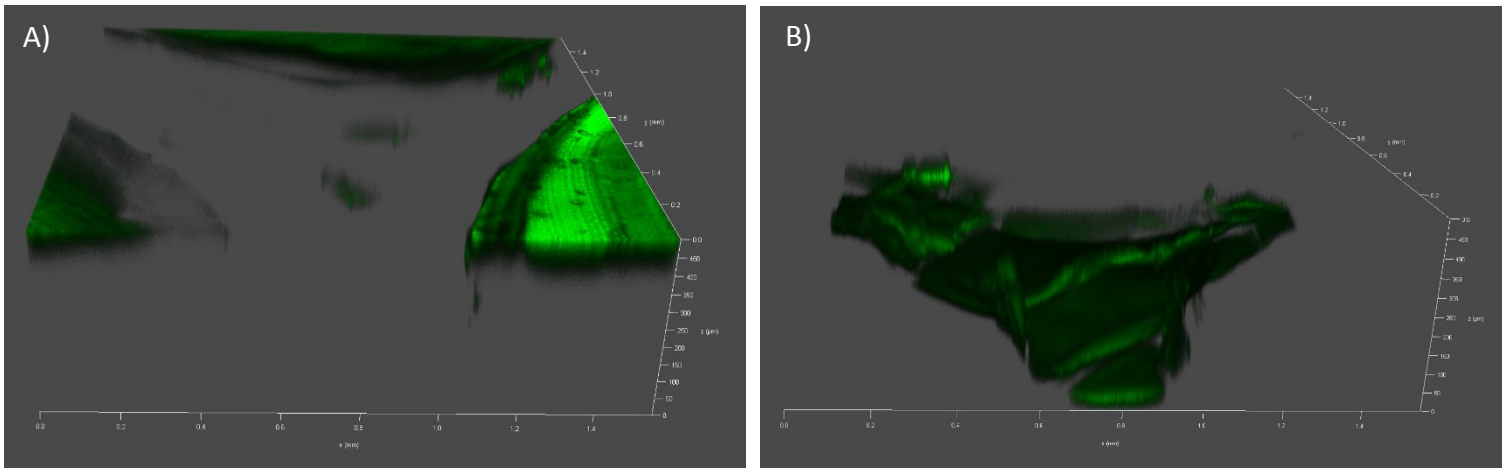

Figure S5-2: A) Top and B) down view by S4 Confocal laser scanning microscope of the ROI 1

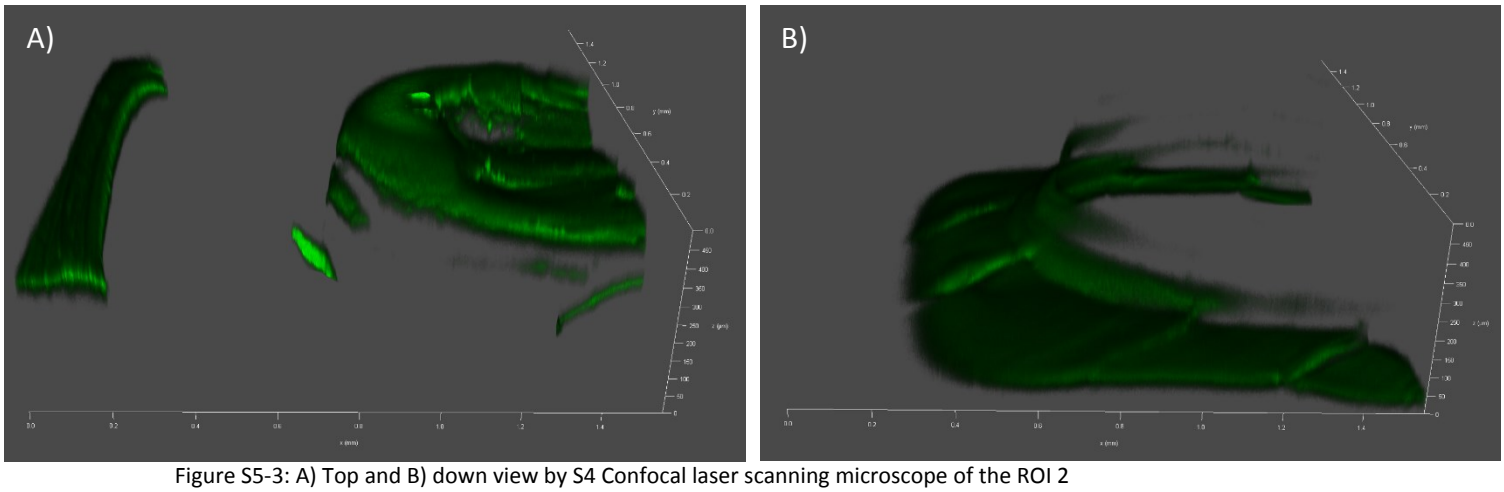

Figure S5-3: A) Top and B) down view by S4 Confocal laser scanning microscope of the ROI 2

S6 Statistical analysis

As explained in the text, different statistical tools have been used to compare LNC formulated with (i) the PEEK and Si/Glass chips and (ii) the PEEK chip with two different flowrates. The objective was to determine if the chip material and the flowrate had any impact on the formulated LNCs.
Three complementary methods are used:

1. Violin plots allow a graphical representation of the raw data, median and interquartile range of each variable, visually showing any significative difference;
2. Passing-Bablok regression check the hypothesis of supposed linearity between the two variables Y_i and X_i ($Y_i = \alpha + \beta X_i$);
3. Bland-Altman plot check the agreement of obtained measures and allow detecting any incoherent value.

- PEEK vs Si/Glass

To compare the two different chips, Si/Glass chip has been selected as the reference chip (X_i) due to the best control of the width and wall linearity of its channels (the PEEK chip being Y_i).

The Passing-Bablok regression study confirms the absence of significative difference between the PEEK and the Si/Glass chips. Indeed, Figure S6-1 shows that the slope is nearly one, and the confidence interval (CI) upper and lower bounds surround the value 1, meaning there is no proportional error. Furthermore, for the intercept, CI bounds surround the value 0, meaning there is no systematic error.

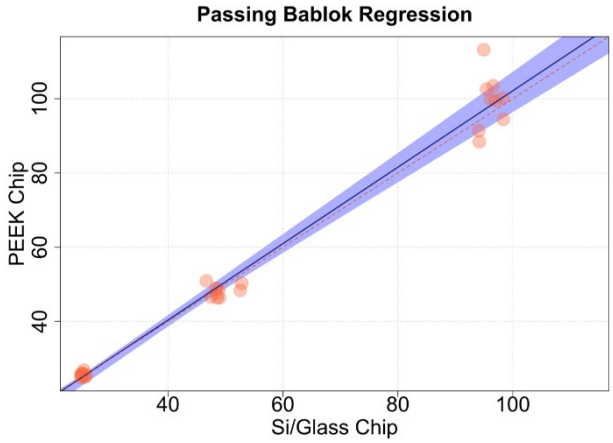

	Est*	LCI*	UCI*
Intercept (α)	-0.831	-4.247	1.685
Slope (β)	1.030	0.947	1.101

*Est: estimated value; LCI: 95% lower confidence interval; UCI: 95% upper confidence interval

Figure S6-1: Sizes of the LNC formulated with PEEK vs Si/Glass chips. Symbols represent experimental couples. The full line shows a Passing-Bablok Regression and the dotted line figures out the identity relation. Size are in nm. The 95% confidence bounds are calculated by the boostrap method (colored area).

In order to consolidate this result, a Bland-Altman analysis has been used to compare result agreement (Figure S6-2). It shows, for each targeted size, in ordinate the size difference (X_i - Y_i) and in abscissa the average size (X_i + Y_i)/2 obtained for a specific condition. It shows a good homogeneity and dispersion of the obtained sizes for all the targeted sizes. However, this analysis highlights the presence of an incoherent result: one of the LNC 100 formulations with Si/Glass chip had a size above 110 nm, while all the other sizes are below 103 nm. Excluding

this specific point, all measurements are within 10% around the median, and even within 5% for the LNC 25.

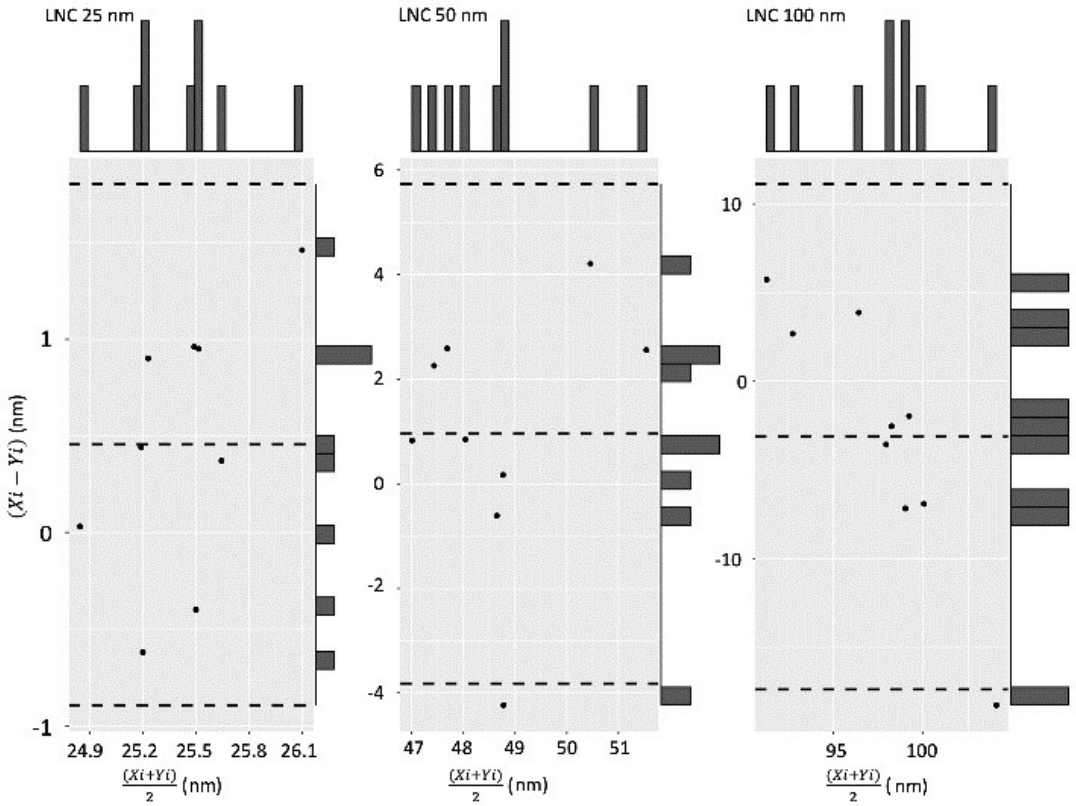

Figure S6-2: Bland-Altman analysis (Si/Glass vs PEEK) for each targeted size (25, 50 and 100 nm). The abscissa axis represents the average size (X_i+Y_i)/2 (with X_i for Si/Glass size and Y_i for PEEK size). The ordinate axis represents the size difference (X_i - Y_i) obtained for a specific condition *i*. Bar charts on the right and the top show the occurrence of those values. Upper and lower Dashed lines represent the upper and lower bound of the 95% confidence interval.

- Low vs High flow rate

To go further in the perspective of a "scaled-up" production, the same analysis was carried out to compare two different flow rates. An increase by a factor 5 was tested. Going above that value could damage chips and trigger leaks. Low flow rate (2.1 m/min) has been selected as the reference (X_i), while the high flow rate (10.5 ml/min) is Y_i.

Figure S6-3 compares results obtained for *D*Hz and PDI at two total flow rates (2.1 mL/min for the lowest and 10.5 mL/min for the highest). Results for LNC 25 suggest no significant difference for sizes and PDI. Same observations can be done for LNC 50 and LNC 100 PDI, but this is less obvious for sizes: LNCs formulated with high flow rate seem slightly smaller than at low flow rate for targeted size over 50 nm.
Passing-Bablok regression (Figure S6-4) confirms the previous observation: with a slope value lower than 1 (between 0.961 and 0.996), a (small) proportional error is attested. However, the intercept value demonstrates the absence of systematic error. Thus, it appears that sizes are slightly smaller when increasing the flow rate, but this drop stays below 5%, which is acceptable.
Bland-Altman analysis (Figure S6-5) shows once again a good homogeneity and dispersion of the obtained sizes for all LNCs, with all measurements within 6% around the median.

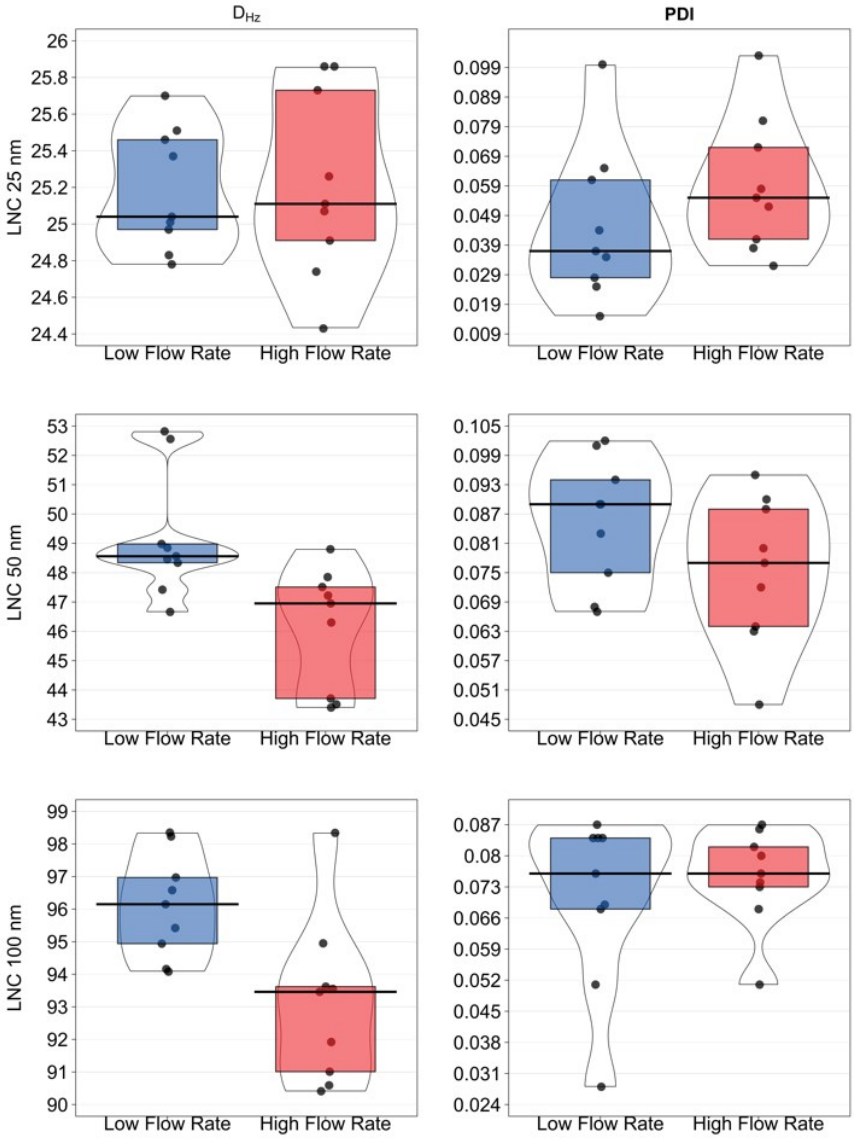

Figure S6-3: Violin plots of DHz and PDI for LNCs formulations obtained with PEEK chip at low (2.1 ml/min) and high flow rate (10.5 ml/min). Each boxplot introduces four elements: black points represent raw data, the horizontal black line represents the median, the bean represents a smoothed density and colored rectangles represent the interquartile range.

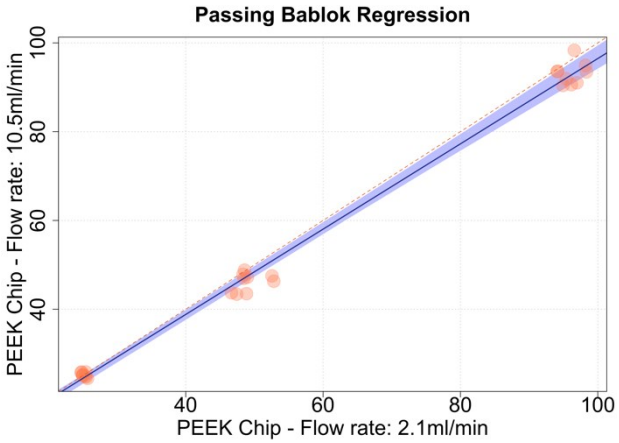

	Est	LCI	UCI
Intercept	-0.382	-1.477	1.902
Slope	0.961	0.927	0.996

*Est: estimated value; LCI: 95% lower confidence interval; UCI: 95% upper confidence interval

Figure S6-4: Sizes of the LNC formulated with high vs low flow rates. Symbols represent experimental couples. The full line shows a Passing-Bablok Regression and the dotted line figures out the identity relation. Size are in nm. The 95% confidence bounds are calculated by the bootstrap method (colored area).

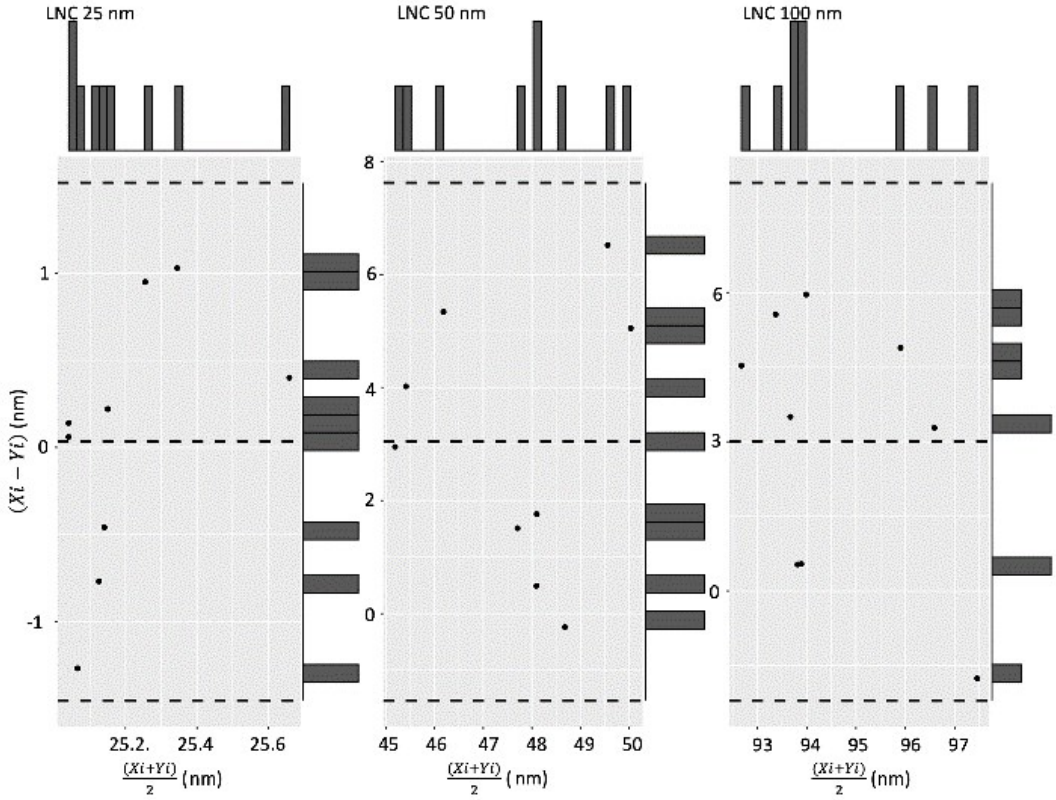

Figure S6-5: Fig 13: Bland-Altman analysis (low vs high flow rate) for each targeted size (25, 50 and 100 nm). The abscissa axis represents the average size (X_i+Y_i)/2 (with X_i for low and Y_i for high flow rate sizes). The ordinate axis represents the size difference (X_i - Y_i) obtained for a specific condition *i*. Bar charts on the right and the top show the occurrence of those values. Upper and lower Dashed lines represent the upper and lower bound of the 95% confidence interval.

S7 Small Angle X-ray Scattering (SAXS) data treatment and comparison

Well-known LNC-PIC batch suspensions were used to collect their SAXS intensity signal using classical glass-borosilicate capillaries with 1.5 mm diameter and 10 µm thick walls. Figure S7-1A shows the raw intensity data (in arbitrary units, a.u.) plotted on a log-log scale and obtained after radial averaging from the 2D detector multiple acquisitions (time averaged 10 × 500 ms), using a mask for the beam stop position that blocks the transmitted beam and dead pixels. A correction was used for pixels different efficiencies. Background measured with the X-ray shutter closed was negligible. SAXS intensity curves, plotted as a function of the scattering vector Q (in $Å^{-1}$), were obtained applying the standard beam-line corrections to reach an absolute scale (i.e. scattering cross section per scattering volume, in cm^{-1}) based on the measurement of the reference scattering intensity of pure water. The green symbols and curve in Figure S7-1A correspond to the raw measurements within 6% around the median and is mostly due to air and instrument window scatterings. For diluted samples, such contributions dominate all the intensity curves at low Q values. The water filled capillary raw signal (blue symbols and curve) is shown on the Figure S7-1A as well as the reference water signal (light grey symbols and curve around 0.0168 cm^{-1}) obtained after subtraction of the glass capillary signal and other beam-line corrections to obtain cm^{-1} units. Similarly, the SAXS signal in $cm^{-1}$of an LNC 25 nm PIC batch suspension diluted at 1% (w/w) was also plotted (red symbols and curve). The sample holder and solvent scattering (water isothermal compressibility signal) are mainly responsible for the scattering at large Q values and were subtracted from the data.

In order to compare the SAXS signal from diluted LNC suspensions measured in the microfluidic chip and in classical capillaries, the same suspension was measured in both environments at rest. The microfluidic chip was totally filled with the suspension used previously, and measurements were carried out through the microfluidic chip in the channel section accessible after the Y junction. The raw signal is plotted with black symbols and line in Figure S7-1B and it is identical to the one measured within capillaries in the low Q range (Figure S7-1A). On the contrary, the large Q range shows a slightly higher intensity due to an increase of the cell wall contribution and solvent scattering amount. Nevertheless, the same trend appears for the raw signal measured within the microfluidic chip filled with pure water (blue symbols and line), so that after subtraction of all these contributions (air, instrument windows scattering, sample holder and solvent scattering), the LNC SAXS curve measured within the microfluidic chip is identical to the one measured in the capillary (Figure S7-1). The best fits to the SAXS data are plotted with solid lines on top of the corresponding data. The model used is based on a spherical particle with a core-shell structure form factor and a hard sphere model for inter particles interactions using the Percus-Yevick closure structure factor. Excellent fits were obtained with a fixed electron density for the solvent (0.334 $Å^{-3}$) and the resulting electron density profile is plotted in Figure S6-2A. Moreover, the model also fits the size distribution of the core radius and shell thickness in the form of a log-normal and a normal distribution respectively (see Figure S6-2B). Lastly, data are in agreement with other experimental LNC determination, such as calculated electron densities from pure materials and sample composition (Table S7-1: reference values calculated for the pure formulation ingredients that composes the samples of the SAXS analysesTable S7-1).

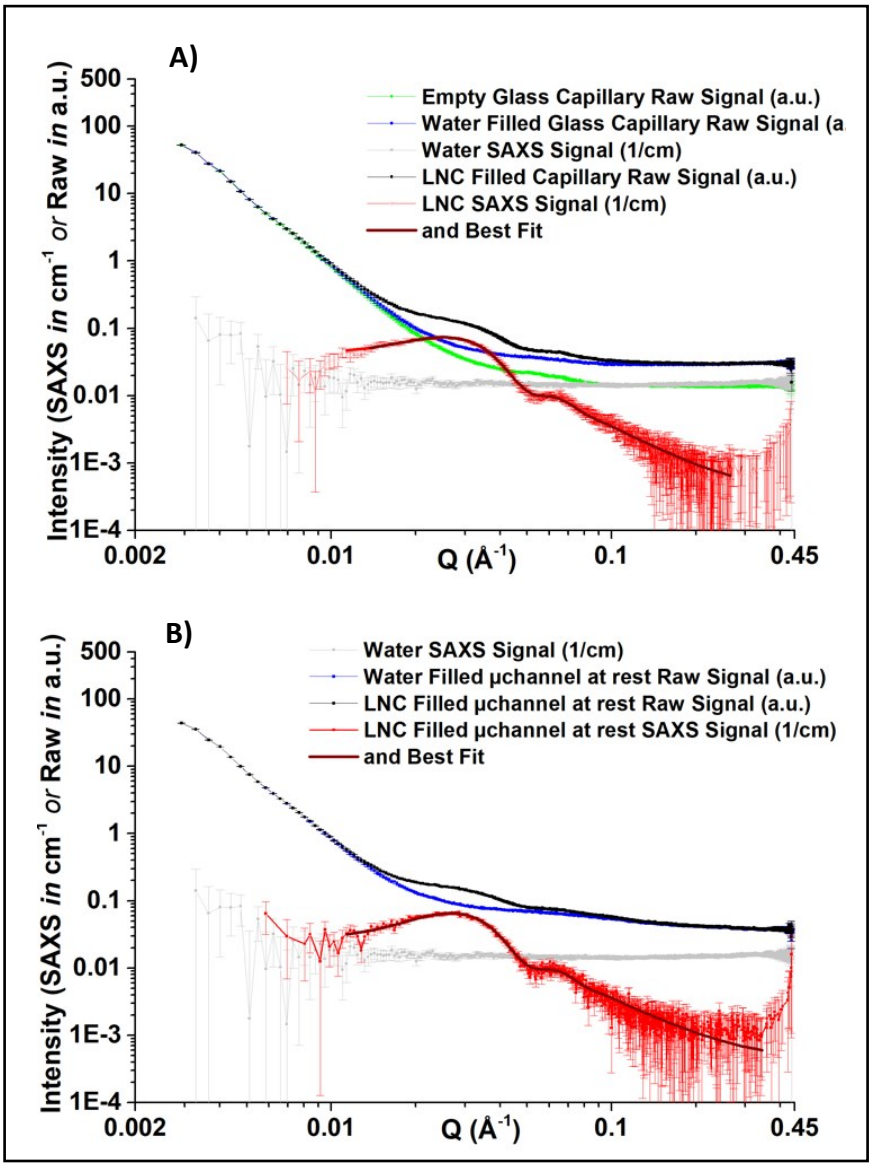

Figure S7-1: A) SAXS raw signal (a.u.) and SAXS intensity (in absolute scale units, cm-1) curves plotted as a function of the scattering vector on a log-log scale for measurements carried out within classical borosilicate glass capillaries (black and red dots, respectively). The black curve is the raw signal of the LNC 25 nm suspension at 1% (w/w). The Blue and green curves correspond for all plots to the raw signal collected with pure water and for air, respectively. The grey curve corresponds to measured pure water scattering in cm^{-1} and is plotted on all graphs as a guide to the eyes; B) corresponds to the same suspensions measured at rest in the microfluidic channel of the Si/Glass chip, 4 mm away from the Y junction (see Fig. 4C). The blue curve raw signal corresponds to the water filled channel and the black curve to the raw signal of the LNC suspension. In both cases, after proper treatments, the LNC suspension SAXS curve was obtained and plotted in red with its best fit to the data (black line).

Table S7-1: reference values calculated for the pure formulation ingredients that composes the samples of the SAXS analyses

Molecule, Segment	***Composition***	***M, Molar mass (g/mol)***	***d*, Volume density ($g.cm^{-3}$)**	***X-ray* (λ=1Å) ρb, Scattering length density ($x10^{-6}Å^{-2}$)**	***X-ray* (λ=1Å) ρ_e, Electron density ($Å^{-3}$)**
Water	**2H;O**	**18.015**	**0.998**	**9.42**	**0.334**
Oil (Labrafac, *WL1349*)	**22H;14C;6O**	**302.15**	**0.945**	**8.64**	**0.307**
hydrophilic segment	5H;6C;6O		1.1	9.62	0.341
hydrophobic segments	17H;8C		0.684	6.67	0.237
Surfactant (Kolliphor HS15)	**96H ;48C ;17O**	**944.53**	**1.048**	**9.8**	**0.348**
hydrophilic segment	61H ;31C ;17O	239.19	1.116	10.3	0.366
hydrophobic segments	35H ;17C	705.34	0.847	8.23	0.292
Co-Surfactant (Span 80)	**44H;24C;6O**	**428.6**	**0.986**	**9.23**	**0.328**
hydrophilic segment	11H;7C;6O	191.08	1.03	9.25	0.328
hydrophobic segments	33H;17C	237.2	0.95	9.18	0.326

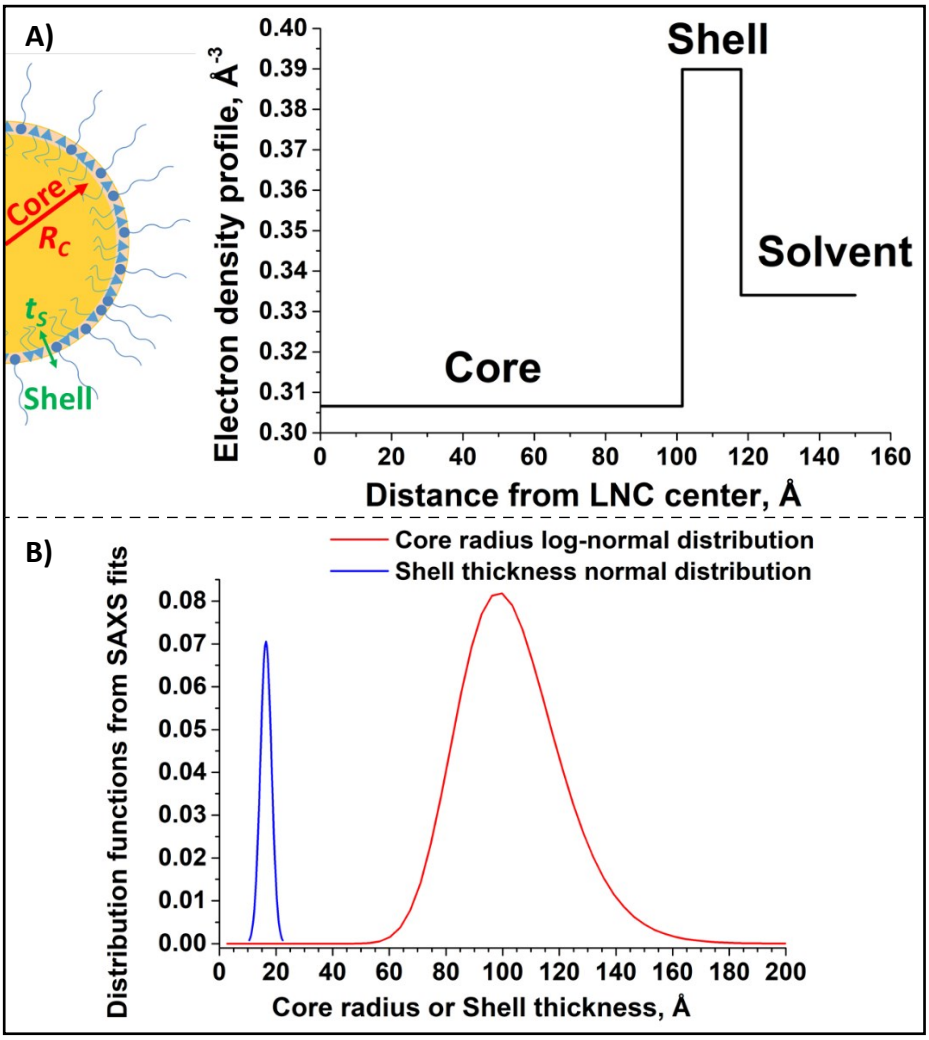

Figure S7-2: A) Electron density profile corresponding to the fit presented in Figure S7-1A for diluted LNC 25nm particles with a sketch representing a LNC; B) Distribution functions obtained from the fit, for the core radius (log-normal distribution) and shell thickness (normal distribution).